SCIENCE CHINA
Information Sciences

• RESEARCH PAPER •

January 2020, Vol. 63 112207:1–112207:13
https://doi.org/10.1007/s11432-019-1470-x

Unscented Kalman-filter-based sliding mode control for an underwater gliding snake-like robot

Jingge TANG[1,2,3], Bin LI[1,2], Jian CHANG[1,2*] & Aiqun ZHANG[1,2]

[1]*State Key Laboratory of Robotics, Shenyang Institute of Automation, Chinese Academy of Sciences, Shenyang* 110016, *China;*
[2]*Institutes for Robotics and Intelligent Manufacturing, Chinese Academy of Sciences, Shenyang* 110169, *China;*
[3]*University of Chinese Academy of Sciences, Beijing* 100049, *China*

Received 22 April 2019/Revised 11 June 2019/Accepted 10 July 2019/Published online 24 December 2019

Abstract With its strong endurance and high maneuverability, an underwater gliding snake-like robot (UGSR) is a strong potential candidate for aquatic exploration and monitoring. The major feature of the UGSR, which distinguishes it from other snake-like robots, is long range and long operation duration by gliding. This study establishes a gliding motion control system for the UGSR based on a sliding mode controller (SMC). The control system stabilizes the system and suppresses the uncertainties and unknown disturbances. In this strategy, chattering is reduced based on the reaching law method. To circumvent the difficulty of velocity measurements, a nonlinear observer based on an unscented Kalman filter (UKF) is employed for state estimation and random noise handling. The effectiveness of the proposed controller and observer is verified by simulating the UKF-based SMC closed-loop system.

Keywords underwater gliding snake-like robot, sliding mode control, reaching law, nonlinear observer, unscented Kalman filter, robustness

Citation Tang J G, Li B, Chang J, et al. Unscented Kalman-filter-based sliding mode control for an underwater gliding snake-like robot. Sci China Inf Sci, 2020, 63(1): 112207, https://doi.org/10.1007/s11432-019-1470-x

1 Introduction

The increased demand for underwater exploration, observation, and monitoring has inspired several underwater vehicles [1, 2] that can probe aquatic environments. The underwater glider is a buoyancy-driven underwater vehicle characterized by high efficiency, long range, and strong endurance. Owing to these properties, underwater gliders are extensively used in real-time monitoring of marine environments. Gliders such as Slocum [3], Spray [4], Seaglider [5], and Sea-Wing [6], have been commercially promoted. However, underwater gliders are disadvantaged by low maneuverability, high cost, and low efficiency in shallow water. With the development of bionics, researchers have turned their attention to bio-inspired underwater robots [7, 8]. An underwater snake-like robot is a bionic underwater vehicle with a chain structure, which adopts multiple swimming gaits by changing its body shape. Although benefiting from many degrees of freedom (DOF) and strong maneuverability [9, 10], the short range and poor endurance have limited the practical application of these and other bio-inspired robots [11]. Recently, researchers have integrated the innovations and technologies of traditional and bionic underwater robots to improve the shortcomings of the existing robots. Sverdrup-Thygeson et al. [12] and Kelasidi et al. [13] equipped an underwater snake-like robot with the propellers of an autonomous underwater vehicle, which improved the locomotion capabilities of the robot in narrow regions. Zhang et al. [14] combined an underwater

* Corresponding author (email: changjian@sia.cn)

glider with a fish robot, achieving the dual benefits of energy efficiency by gliding and high mobility by fish-like swimming. Wu et al. [15] studied a gliding robotic dolphin in which the gliding attitude angles can be adjusted through the pectoral, caudal, and dorsal fins. Inspired by hybrid-driven underwater bio-robots, the present study proposes an underwater gliding snake-like robot (UGSR) that combines the advantages of underwater gliders and underwater snake-like robots. The robot design achieves both gliding and snake-like swimming in shallow waters such as rivers and lakes. The gliding motion is realized by adjusting the net buoyancy and pitch moment in the vertical plane. As energy is consumed only during state adjustment, the robot operates for long durations with low energy consumption. Meanwhile, swimming is realized by continuous body deformation through a series of rotating joints. Different joint functions provide different locomotion gaits providing flexible and maneuverable movements. This study focuses on the gliding motion.

When developing the UGSR, the buoyancy and pitch adjustment mechanisms must be integrated into a general underwater robotic snake. However, the pump devices installed in underwater gliders [3–6] are difficult to install in the limited internal space of a slender body with a modular structure. Instead, a telescopic module is designed for the UGSR. A screw mechanism in this mechanism adjusts the length of the telescopic module, providing the net buoyancy and pitch adjustment system for gliding.

Control strategies for gliding motion in the vertical plane have adopted linear proportional-integral-derivative (PID) controller [16], linear-quadratic regulator (LQR) controller [17], and model-based nonlinear controllers [18, 19]. However, the control algorithms of gliding motion are typically designed for movable-mass underwater gliders, and have rarely been studied for variable-length gliding systems. This paper employs a sliding mode controller (SMC) for stable gliding tracking and robust control under external disturbance and parameter perturbations [20–22]. The discontinuity in this strategy, which causes chattering with consequent performance loss and system instability, is alleviated by the reaching law method [23]. The proposed method controls the characteristics of the reaching mode and the amplitude of the chattering. As the robot velocity is difficult to measure in water, a state observer that estimates the real-time state of the system is designed. To measure the pitch angle in the presence of sensor noise, the observer must extract the useful data from a noisy signal and estimate the system state. Zhang et al. [24] designed a nonlinear observer with an extended Kalman filter, which is vulnerable to linear error divergences. Yuan et al. [25] estimated the system state by a sliding mode observer, which is robust to uncertainty and disturbance but sensitive to measurement noise. In this paper, the state is estimated by a nonlinear observer built by the unscented Kalman filter (UKF) method [26]. The UKF solves nonlinear transfer problems of the mean and covariance by an unscented transformation, achieving high accuracy and robustness to measurement noise. Because it considers the nonlinear characteristics of system control and state estimation, the UKF-based SMC system improves the robustness of the system against disturbances and measurement noise.

The remainder of this paper is organized as follows. Section 2 describes the implementation of the UGSR prototype, and Section 3 derives the dynamic model of gliding motion in the vertical plane. Section 4 derives the input-output linearization of the model, and obtains its normal form. The system control law designed by the SMC method, and the nonlinear observer designed by the UKF method, are also introduced in this section. Finally, the proposed controller and observer are verified by simulations in Section 5.

2 Prototype of the UGSR

This section describes the development and implementation of the UGSR prototype. Figure 1 shows the gliding motion and snake-like swimming of the robot during pool tests.

The UGSR has a serial structure composed of multiple telescopic and rotate modules (see Figure 2). Each telescopic module has three DOFs, namely, telescoping, pitch, and yaw. The net buoyancy can be adjusted by controlling the length of the telescopic module. A pitch moment is generated when the telescopic modules symmetrically installed at both ends of the robot are unequal in length. The net

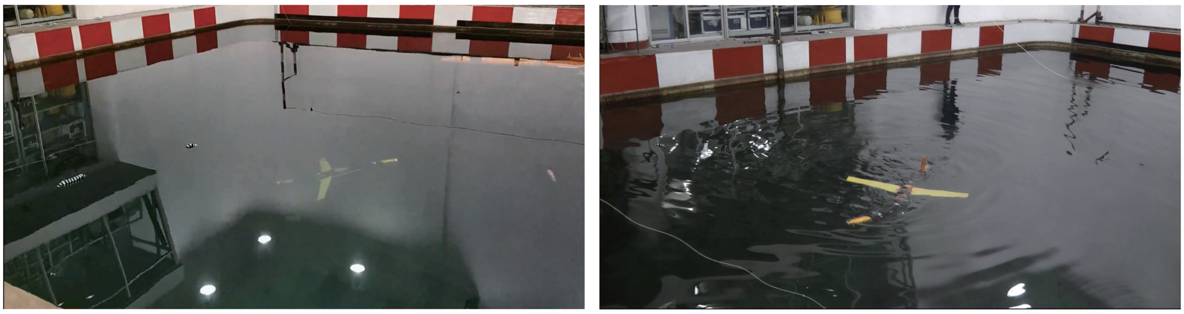

(a) (b)

Figure 1 (Color online) Test of the UGSR in a pool. (a) Gliding; (b) swimming.

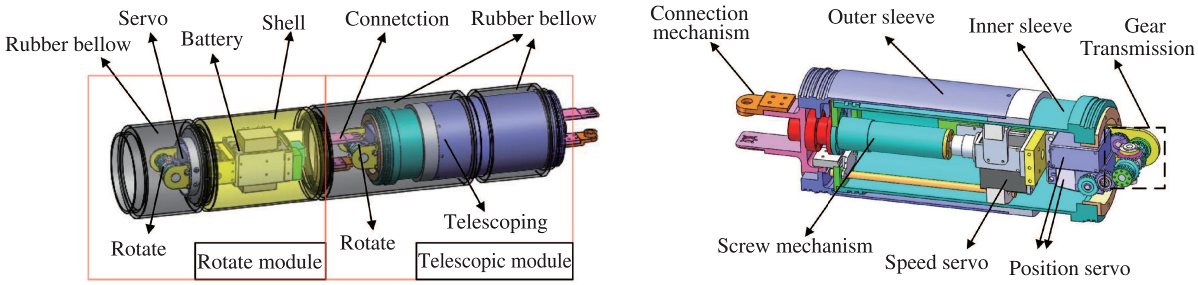

(a) (b)

Figure 2 (Color online) Modules of the UGSR. (a) Structures of the rotate and telescopic modules; (b) composition of the telescopic module.

Table 1 Hardware and parameters of the developed prototype

Name	Description	Parameter	Value
Position servo	JRFROPO DS6315HV	Length of telescopic module (m)	0.4
Speed servo	Futaba BLS172SV	Length of rotate module (m)	0.25
Hull	7050 aluminum alloy	Diameter (m)	0.12
Seal	O-ring, rubber bellow, clamp, thread groove	Total length (m)	1.8
Pressure sensor	Bar02	Total mass (kg)	7.9
Attitude sensor	JY901	Elongation range (m)	$[-0.05, 0.05]$

buoyancy and pitch moment are coupled, as both are related to the elongations of the two telescopic modules. The UGSR is upwardly gliding in Figure 1(a). The rotate module has two DOFs, namely, pitch and yaw. When all rotate joints of the robot change continuously according to different joint functions, the robot achieves a variety of swimming gaits, such as serpentine and lateral locomotions. In Figure 1(b), the UGSR is turning right while swimming.

To meet the linear displacement and angular position demands of the modules, a speed servo and position servo are used as system drivers. The module shell is made of aluminum alloy, which resists the pressure at 20 m water depth. The space between the modules is sealed by O-rings, rubber bellows, and clamps, and both end caps are sealed by O-rings and thread grooves. The module length is precisely controlled by a linear potentiometer mounted on each telescopic module. In addition, the depth information is controlled by a pressure sensor installed on the head, and the pitch angle data are acquired in real-time by an attitude sensor. The specifics of the hardware are given in Table 1.

The developed UGSR prototype is composed of two telescopic modules and four rotate modules. Their parameters are listed in Table 1.

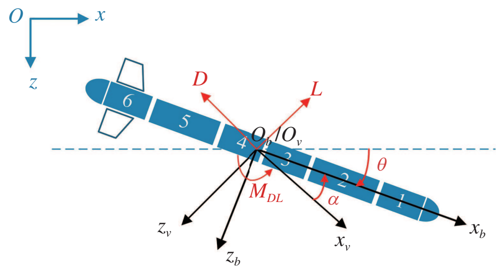

Figure 3 (Color online) Representation of coordinate systems in the vertical plane.

3 Modeling of gliding motion in the vertical plane

This section derives the dynamic model of gliding motion in the vertical plane. The model is simplified by the following assumptions: (1) the robot is submerged in water and neutrally buoyant; (2) the robot does not move in the lateral direction; (3) the joint angles of all rotate joints are zero.

The coordinate systems are defined using the right-hand rule in Figure 3. The world coordinate system, represented by $Oxyz$, is located at a fixed point, so the initial displacement of the robot is zero. The Ox and Oz axes lie in the forward direction and the gravitational acceleration direction, respectively. The body coordinate system, denoted by $O_bx_by_bz_b$, is initially located in the geometric center of the body. Its position coordinates with respect to $Oxyz$ along the Ox and Oz axes are expressed as x and z, respectively. O_bx_b is aligned with the longitudinal axis of the body and points to the head module, whereas O_bz_b is perpendicular to O_bx_b and points downward in the vertical plane. The origin of the velocity coordinate system $O_vx_vy_vz_v$ coincides with the origin of $O_bx_by_bz_b$. The O_vx_v axis aligns along the direction of the velocity with magnitude V, and O_vz_v is normal to the O_vx_v axis. The angle between Ox and O_bx_b is the pitch angle θ, and the angle between O_vx_v and O_bx_b is the angle of attack α. Counterclockwise pitch and attack angles are regarded as positive. In Figure 3, θ is negative and α is positive. The gliding path angle γ defines the angle between Ox and O_vx_v. The three angles are related by $\theta = \gamma + \alpha$. The kinematic model is then easily obtained as

$$\dot{x} = V\cos\gamma, \quad \dot{z} = -V\sin\gamma.$$

The robot consists of 6 modules, numbered $j = 1, 2, \dots, 6$ from head to tail. The elongations of telescopic modules 2 and 5 are represented by δ_2 and δ_5, respectively. The mass and volume of module j are expressed as m_j and q_j, respectively. Assuming uniform density of each module, the center of mass locates at the centroid, represented by r_j with respect to frame $O_bx_by_bz_b$. An additional mass m_h, located at position r_h along O_bz_b, facilitates self-stability by keeping the center of gravity (CG) below the center of buoyancy (CB). Defining the fluid density as ρ, the displaced water mass is calculated as $m = \rho \sum q_j$. The net buoyancy, expressed as the total mass minus the displaced mass, is given by $m_0 = \sum m_j + m_h - m$. The positions of CG and CB, represented by r_g and r_b respectively, are written as follows:

$$r_g = \frac{\sum m_j r_j}{\sum m_j}, \quad r_b = \frac{\sum q_j r_j}{\sum q_j}, \quad j = 1, 2, \dots, 6.$$

The external forces and moments acting on the robot are generated by the masses, buoyancy, and hydrodynamics. The gravity is denoted by $G = \sum m_j g + m_h g$, where g is the gravitational acceleration. The buoyancy is denoted by $B = -mg$, where m varies with δ_2 or δ_5. As the r_g and r_b are functions of the elongations δ_2 or δ_5, moments are exerted by gravity and buoyancy if $\delta_2 \neq \delta_5$. These moments are described as

$$T_g = \sum m_j g r_g \cos\theta - m_h g r_h \sin\theta, \quad T_b = -mgr_b\cos\theta.$$

Hydrodynamic forces and moments are generated when the body moves through the fluid. The force is resolved into its drag D and lift L components, which are parallel and perpendicular to the velocity direction in the vertical plane, respectively (see Figure 3). The pitching moment of the couple is indicated by M_{DL}. Based on aircraft dynamics, the hydrodynamics of the drag, lift and moment are modeled in terms of the variables α and V

$$D = (C_{D0} + C_D\alpha^2)V^2, \quad L = (C_{L0} + C_L\alpha)V^2, \quad M_{DL} = (C_{M0} + C_M\alpha + C_q\omega_2)V^2,$$

where C_{D0}, C_D, C_{L0}, C_L, C_{M0}, C_M and C_q are hydrodynamic coefficients obtained by a computational fluid dynamics simulation, and ω_2 is the angular velocity of θ.

The dynamic model of gliding motion for the UGSR is given by

$$\begin{aligned} &\dot{V} = \frac{1}{M_1}(-D - g\sin\gamma m_0), \quad \dot{\gamma} = \frac{1}{M_1 V}(L - g\cos\gamma m_0),\\ &\dot{\alpha} = \omega_2 - \frac{1}{M_1 V}(L - g\cos\gamma m_0), \quad \dot{\omega}_2 = \frac{1}{J_2}(M_{DL} + T_g + T_b), \end{aligned} \tag{1}$$

where the mass M_1 along the $O_b x_b$ axis is assumed equal to the mass along $O_b z_b$. J_2 is the moment of inertia about $O_b y_b$, including the stationary and added masses and neglecting the rotational inertia caused by the length change of the telescopic modules.

Under the first assumption, the net buoyancy can be written as $m_0 = -\rho\pi r^2(\delta_2 + \delta_5)$, where r is the radius of the body. In addition, the expression $T_g + T_b$ is a quadratic function of δ_2 and δ_5. For the controller design, the system is rendered more concise and convenient by introducing two parameters u_1 and u_2 describing the system inputs.

$$u_1 = m_0, \quad u_2 = \sum m_i r_g - m r_b. \tag{2}$$

The system dynamics (1) are then written as follows:

$$\dot{\boldsymbol{X}} = \boldsymbol{f}(\boldsymbol{X}) + \boldsymbol{g}(\boldsymbol{X})\boldsymbol{u} + \boldsymbol{w}, \quad \boldsymbol{y} = \boldsymbol{h}(\boldsymbol{X}), \tag{3}$$

where $\boldsymbol{X} = [V, \gamma, \alpha, \omega_2]^{\mathrm{T}}$ is the state vector, $\boldsymbol{u} = [u_1, u_2]^{\mathrm{T}}$ is the system input, $\boldsymbol{w}$ embodies the uncertainty and unknown disturbance, and $\boldsymbol{y}$ is the system output. The system functions $\boldsymbol{f}(\boldsymbol{X})$, $\boldsymbol{g}(\boldsymbol{X})$ and $\boldsymbol{h}(\boldsymbol{X})$ are expressed as

$$\boldsymbol{f}(\boldsymbol{X}) = \begin{bmatrix} -\dfrac{1}{M_1}D \\ \dfrac{1}{M_1 V}L \\ \omega_2 - \dfrac{1}{M_1 V}L \\ \dfrac{1}{J_2}(M_{DL} - m_h r_h g\sin(\gamma+\alpha)) \end{bmatrix}, \quad \boldsymbol{g}(\boldsymbol{X}) = \begin{bmatrix} -\dfrac{g\sin\gamma}{M_1} & 0 \\ -\dfrac{g\cos\gamma}{M_1 V} & 0 \\ \dfrac{g\cos\gamma}{M_1 V} & 0 \\ 0 & \dfrac{g}{J_2}\cos(\gamma+\alpha) \end{bmatrix}, \quad \boldsymbol{h}(\boldsymbol{X}) = \begin{bmatrix} h_1 \\ h_2 \end{bmatrix} = \begin{bmatrix} V\cos\gamma \\ \gamma + \alpha \end{bmatrix}.$$

4 Design of the controller

This section establishes the nonlinear control of the desired gliding path. The system (3) is first subjected to input-output linearization to obtain the tracking error dynamics. Next, for stability and consistency in the case of parameter uncertainty and unknown disturbance, the feedback control law is obtained by SMC based on the reaching law method. The module elongations δ_2 and δ_5, which constitute the actual system inputs, are then obtained by the decoupling expression (2). To apply the closed-loop control, all system states are required as the feedback inputs of the controller. However, obtaining the velocity in real-time is a challenging task. The pitch angle θ of the UGSR is easily measured by the attitude sensor, but the measured data differ from the true result due to the measurement noise. Instead, filtering and state estimation are performed by a nonlinear observer employing the UKF method. Figure 4 is a diagram of the overall control system based on the SMC and UKF. The estimated state is represented by the hat symbol $\hat{\boldsymbol{X}} = [\hat{V}, \hat{\gamma}, \hat{\alpha}, \hat{\omega}_2]^{\mathrm{T}}$. The symbols $\boldsymbol{\xi}$ and $\boldsymbol{\xi}_d$ represent the system state and its desired value in the linearized system, respectively.

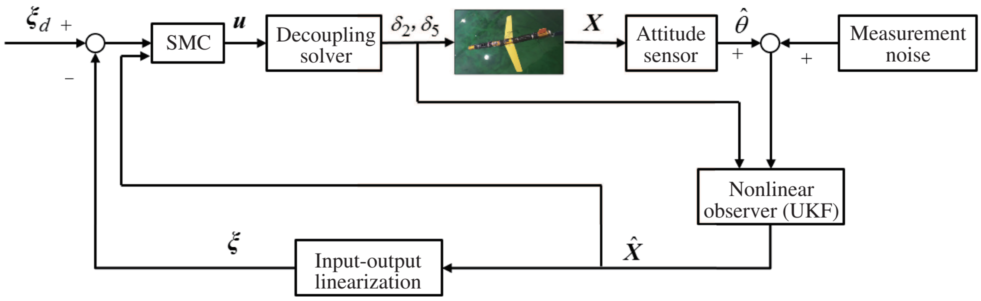

Figure 4 (Color online) Diagram of the UKF-based SMC system.

4.1 Input-output linearization

The derivative of the output of the system (3) is given by

$$\dot{\boldsymbol{y}} = \frac{\partial \boldsymbol{h}}{\partial \hat{\boldsymbol{X}}}[\boldsymbol{f}(\hat{\boldsymbol{X}}) + \boldsymbol{g}(\hat{\boldsymbol{X}})\boldsymbol{u}] = L_{\boldsymbol{f}}\boldsymbol{h} + L_{\boldsymbol{g}}\boldsymbol{h}\boldsymbol{u} = \begin{bmatrix} \frac{1}{M_1}(-\hat{D}\cos\hat{\gamma} - \hat{L}\sin\hat{\gamma}) \\ \hat{\omega}_2 \end{bmatrix},$$

where $L_{\boldsymbol{f}}\boldsymbol{h}$ is the Lie derivative of $\boldsymbol{h}$ with respect to $\boldsymbol{f}$, $\hat{D} = (C_{D0} + C_D\hat{\alpha}^2)\hat{V}^2$, and $\hat{L} = (C_{L0} + C_L\hat{\alpha})\hat{V}^2$. As $L_{\boldsymbol{g}}\boldsymbol{h} = \boldsymbol{0}$, the derivative of $\dot{\boldsymbol{y}}$ is calculated as

$$\boldsymbol{y}^{(2)} = \frac{\partial(L_{\boldsymbol{f}}\boldsymbol{h})}{\partial \hat{\boldsymbol{X}}}[\boldsymbol{f}(\hat{\boldsymbol{X}}) + \boldsymbol{g}(\hat{\boldsymbol{X}})\boldsymbol{u}] = L_{\boldsymbol{f}}^2\boldsymbol{h} + L_{\boldsymbol{g}}L_{\boldsymbol{f}}\boldsymbol{h}\boldsymbol{u} = \begin{bmatrix} L_{\boldsymbol{f}}^2 h_1 + L_{\boldsymbol{g}}L_{\boldsymbol{f}}h_1\boldsymbol{u} \\ L_{\boldsymbol{f}}^2 h_2 + L_{\boldsymbol{g}}L_{\boldsymbol{f}}h_2\boldsymbol{u} \end{bmatrix},$$

where

$$\begin{aligned} L_{\boldsymbol{g}}L_{\boldsymbol{f}}h_1\boldsymbol{u} &= \frac{1}{M_1^2\hat{V}}\left[g\hat{D}\cos\hat{\gamma}\sin\hat{\gamma} + 2g\hat{L}\sin^2\hat{\gamma} + g\hat{L}\cos^2\hat{\gamma} - 2gC_D\hat{\alpha}\hat{V}^2\cos^2\hat{\gamma} - gC_L\hat{V}^2\sin\hat{\gamma}\cos\hat{\gamma}\right]u_1, \\ L_{\boldsymbol{g}}L_{\boldsymbol{f}}h_2\boldsymbol{u} &= \frac{g}{J_2}\cos(\hat{\gamma} + \hat{\alpha})u_2. \end{aligned}$$

As the first derivative of $\boldsymbol{y}$ is independent of $\boldsymbol{u}$ but the second derivative depends on $\boldsymbol{u}$, the relative degree of the system (3) is $\boldsymbol{\rho}_r = [2, 2]^{\mathrm{T}}$. Therefore, the diffeomorphism $\boldsymbol{T}(\hat{\boldsymbol{X}})$ that transforms the original $\hat{\boldsymbol{X}}$ system into the new $\boldsymbol{\xi}$ system can be written as

$$\boldsymbol{\xi} = \boldsymbol{T}(\boldsymbol{X}) = \begin{bmatrix} h_1 \\ \dot{h}_1 \\ h_2 \\ \dot{h}_2 \end{bmatrix} = \begin{bmatrix} \hat{V}\cos\hat{\gamma} \\ \frac{1}{M_1}(-\hat{D}\cos\hat{\gamma} - \hat{L}\sin\hat{\gamma}) \\ \hat{\gamma} + \hat{\alpha} \\ \hat{\omega}_2 \end{bmatrix} = \begin{bmatrix} \xi_1 \\ \xi_2 \\ \xi_3 \\ \xi_4 \end{bmatrix}.$$

The tracking error $\boldsymbol{e}$ in the reference output $\boldsymbol{h}_d$ and its derivative $\dot{\boldsymbol{h}}_d$, where the subscript d indicates the reference signal, is given by

$$\boldsymbol{e} = \begin{bmatrix} \xi_1 - h_{1d} \\ \xi_2 - \dot{h}_{1d} \\ \xi_3 - h_{2d} \\ \xi_4 - \dot{h}_{2d} \end{bmatrix} = \boldsymbol{\xi} - \boldsymbol{\xi}_d = \begin{bmatrix} e_1 \\ e_2 \\ e_3 \\ e_4 \end{bmatrix}.$$

The tracking error dynamics are then expressed as follows:

$$\dot{\boldsymbol{e}} = \begin{bmatrix} e_2 \\ L_{\boldsymbol{f}}^2 h_1 + L_{\boldsymbol{g}}L_{\boldsymbol{f}}h_1\boldsymbol{u} \\ e_4 \\ L_{\boldsymbol{f}}^2 h_2 + L_{\boldsymbol{g}}L_{\boldsymbol{f}}h_2\boldsymbol{u} \end{bmatrix}. \tag{4}$$

4.2 SMC design

The SMC based on the reaching law involves a reaching phase and a sliding phase. The reaching phase drives the system to a stable manifold in finite time, and the sliding phase drives it to the equilibrium point. Among several classical reaching laws, the constant-rate reaching law forces the switching variable to the manifold at a constant rate. An excessively small rate lengthens the convergence time, whereas an excessively large rate causes severe chattering. The proportional-rate reaching law ensures the reaching rate when the sliding variable is large. The power-rate reaching law increases and decreases the reaching rate when the state is far from and nearby the manifold, respectively, achieving fast reaching with low chattering. The sliding variables of the error system (4) are selected as

$$\begin{aligned} s_1 &= c_1e_1 + e_2, \quad c_1 > 0, \\ s_2 &= c_2e_3 + e_4, \quad c_2 > 0. \end{aligned}$$

We then have

$$\begin{aligned} \dot{s}_1 &= c_1\dot{e}_1 + \dot{e}_2 = c_1e_2 + L_{\boldsymbol{f}}^2h_1 + L_{\boldsymbol{g}}L_{\boldsymbol{f}}h_1\boldsymbol{u}, \\ \dot{s}_2 &= c_2\dot{e}_3 + \dot{e}_4 = c_2e_4 + L_{\boldsymbol{f}}^2h_2 + L_{\boldsymbol{g}}L_{\boldsymbol{f}}h_2\boldsymbol{u}. \end{aligned} \tag{5}$$

Considering the characteristics of the above reaching laws and the necessity of fast convergence with minimal chattering, $\dot{s}_1$ and $\dot{s}_2$ are defined in terms of the proportional- and power-rate reaching laws.

$$\begin{aligned} \dot{s}_1 &= -\epsilon_1|s_1|^{b_1}\tanh\left(\frac{s_1}{p_1}\right) - k_1s_1, \quad \epsilon_1 > 0, \quad p_1 > 0, \quad k_1 > 0, \quad 1 > b_1 > 0, \\ \dot{s}_2 &= -\epsilon_2|s_2|^{b_2}\tanh\left(\frac{s_2}{p_2}\right) - k_2s_2, \quad \epsilon_2 > 0, \quad p_2 > 0, \quad k_2 > 0, \quad 1 > b_2 > 0, \end{aligned} \tag{6}$$

where the hyperbolic tangent function $\tanh(\cdot)$ replaces the discontinuous sign function. Substituting (6) into (5), the system control law is obtained as follows:

$$\boldsymbol{u} = \frac{1}{L_{\boldsymbol{g}}L_{\boldsymbol{f}}\boldsymbol{h}\boldsymbol{u}}\left(\begin{bmatrix} -\epsilon_1|s_1|^{b_1}\tanh\left(\dfrac{s_1}{p_1}\right) - k_1s_1 - c_1e_2 \\ -\epsilon_2|s_2|^{b_2}\tanh\left(\dfrac{s_2}{p_2}\right) - k_2s_2 - c_2e_4 \end{bmatrix} - L_{\boldsymbol{f}}^2\boldsymbol{h}\right).$$

The Lyapunov function is defined as

$$V_s = \frac{1}{2}s_1^2 + \frac{1}{2}s_2^2 \geqslant 0.$$

Lemma 1 in [27] states that for every given scalar x and positive scalar p, the inequality $x\tanh(px) = |x\tanh(px)| = |x||\tanh(px)| \geqslant 0$ holds. Then the derivative of V_s is computed as

$$\begin{aligned} \dot{V}_s &= s_1\dot{s}_1 + s_2\dot{s}_2 = -k_1s_1^2 - k_2s_2^2 - s_1\tanh\left(\frac{s_1}{p_1}\right)\epsilon_1|s_1|^{b_1} - s_2\tanh\left(\frac{s_2}{p_2}\right)\epsilon_2|s_2|^{b_2} \\ &\leqslant -k_1s_1^2 - k_2s_2^2 \leqslant -2k_1V_s - 2k_2V_s \leqslant 0. \end{aligned}$$

Meanwhile, Lemma 3.2.4 in [28] states that for f, V: $[0,\infty) \in \mathbb{R}$, and then $\dot{V} \leqslant -aV + f$ $(\forall t \geqslant t_0 \geqslant 0)$. This implies that $V(t) \leqslant \mathrm{e}^{-a(t-t_0)}V(t_0) + \int_{t_0}^{t}\mathrm{e}^{-a(t-\tau)}f(\tau)\mathrm{d}\tau$ for any finite constant a. Thus we have

$$V_s(t) \leqslant \mathrm{e}^{-2k_1(t-t_0)}V_s(t_0) + \mathrm{e}^{-2k_2(t-t_0)}V_s(t_0).$$

This result shows that the closed-loop system is exponentially convergent, and the convergence accuracy depends on k_1 and k_2.

4.3 Nonlinear observer design

The framework of the UKF, which involves the state estimation of a discrete-time nonlinear system, is described as

$$\boldsymbol{X}_{k+1}=\boldsymbol{f}(\boldsymbol{X}_k)+\boldsymbol{g}(\boldsymbol{X}_k)\boldsymbol{u}_k+\boldsymbol{\Delta}_k,\quad Z_k=h_2(\boldsymbol{X}_k)+\sigma_k.$$

In this expression, $\boldsymbol{X}_k$ and $\boldsymbol{u}_k$ are the state vector and input of the system, respectively, and Z_k is the output θ measured by the attitude sensor. $\boldsymbol{\Delta}_k$ and σ_k denote the process and measurement noises, respectively, which are zero-mean Gaussian white noises with covariance matrices $\boldsymbol{Q}$ and R, respectively.

The UKF performs an unscented transformation, which calculates the statistics of a random variable in nonlinear transformations. For an n dimensional random vector $\boldsymbol{x}$ satisfying the nonlinear transformation $y=f(\boldsymbol{x})$, the mean and covariance of $\boldsymbol{x}$ are $\bar{\boldsymbol{x}}$ and $\boldsymbol{P}$, respectively. A matrix χ of $2n+1$ sigma points is then obtained as

$$\begin{aligned}&\chi_0=\bar{\boldsymbol{x}},\\&\chi_i=\bar{\boldsymbol{x}}+(\sqrt{(n+\lambda)\boldsymbol{P}})_i,\quad i=1,\ldots,n,\\&\chi_i=\bar{\boldsymbol{x}}-(\sqrt{(n+\lambda)\boldsymbol{P}})_i,\quad i=n+1,\ldots,2n,\end{aligned}\tag{7}$$

where $(\sqrt{(n+\lambda)\boldsymbol{P}})_i$ is calculated for the i-th column of the matrix square root of $(n+\lambda)\boldsymbol{P}$. Propagating the sigma vectors by a nonlinear function $y_i=f(\chi_i)$, the mean and covariance of y are respectively calculated as

$$\bar{y}=\sum_{i=0}^{2n}W_i^{(m)}y_i,\quad \boldsymbol{P}_y=\sum_{i=0}^{2n}W_i^{(c)}[y_i-\bar{y}][y_i-\bar{y}]^{\mathrm{T}},$$

where W_i is the weight of the related sigma point

$$\begin{aligned}&W_0^{(m)}=\frac{\lambda}{n+\lambda},\\&W_0^{(c)}=\frac{\lambda}{n+\lambda}+1-a^2+\beta,\\&W_i^{(m)}=W_i^{(c)}=\frac{1}{2(n+\lambda)},\quad i=1,\ldots,2n.\end{aligned}$$

The superscripts m and c denote the mean and covariance, respectively. The parameter $\lambda=a^2(n+\kappa)-n$ is the scaling factor. a indicates the distribution of the sigma point with respect to $\bar{\boldsymbol{x}}$, and κ is a secondary scaling parameter. β is a non-negative weight parameter for incorporating the prior knowledge of the $\boldsymbol{x}$ distribution.

The state estimation algorithm proceeds through the following steps:

(1) Initialize the algorithm.

$$\hat{\boldsymbol{X}}_0=E(\boldsymbol{X}_0),\quad \boldsymbol{P}_0=E[(\boldsymbol{X}_0-\hat{\boldsymbol{X}}_0)(\boldsymbol{X}_0-\hat{\boldsymbol{X}}_0)^{\mathrm{T}}].$$

(2) For $i=1,\ldots,2n+1$, select the sigma points based on (7).

$$\boldsymbol{X}_{i,k}=\left[\hat{\boldsymbol{X}}_k\ \ \hat{\boldsymbol{X}}_k+\sqrt{(n+\lambda)\boldsymbol{P}_k}\ \ \hat{\boldsymbol{X}}_k-\sqrt{(n+\lambda)\boldsymbol{P}_k}\right].$$

(3) Process the time-update equations.

$$\begin{aligned}&\boldsymbol{X}_{i,k+1|k}=\boldsymbol{f}(\boldsymbol{X}_{i,k})+\boldsymbol{g}(\boldsymbol{X}_{i,k})\boldsymbol{u}_k,\\&\hat{\boldsymbol{X}}_{k+1}^{*}=\sum_{i=0}^{2n}W_i^{(m)}\boldsymbol{X}_{i,k+1|k},\\&\boldsymbol{P}_{k+1}^{*}=\sum_{i=0}^{2n}W_i^{(c)}[\boldsymbol{X}_{i,k+1|k}-\hat{\boldsymbol{X}}_{k+1}^{*}][\boldsymbol{X}_{i,k+1|k}-\hat{\boldsymbol{X}}_{k+1}^{*}]^{\mathrm{T}}+Q.\end{aligned}$$

Table 2 System parameters in the simulation

Parameter	Value	Parameter	Value
M_1 (kg)	20.2	J_2 (kg $\cdot$ m^2)	5.5118
m_h (kg)	0.03	r_h (m)	0.025
C_D (kg/m/rad^2)	118.2	C_{D0} (kg/m)	3.789
C_L (kg/m/rad)	120.5	C_{L0} (kg/m)	0.11
C_M (kg/rad)	-13.42	C_{M0} (kg)	-0.03041
C_q (kg $\cdot$ s/rad)	-2		

(4) Repeat the unscented transformation to obtain the new sigma points based on the predicted values of the precious step.

$$\boldsymbol{X}_{i,k+1} = \left[\hat{\boldsymbol{X}}^*_{k+1} \quad \hat{\boldsymbol{X}}^*_{k+1} + \sqrt{(n+\lambda)\boldsymbol{P}^*_{k+1}} \quad \hat{\boldsymbol{X}}^*_{k+1} - \sqrt{(n+\lambda)\boldsymbol{P}^*_{k+1}}\right].$$

(5) Process the measurement-update equations.

$$\begin{aligned}
Z_{i,k+1|k} &= h_2(\boldsymbol{X}_{i,k+1}),\\
\bar{Z}_{k+1} &= \sum_{i=0}^{2n} W_i^{(m)} Z_{i,k+1|k},\\
P_{z_k z_k} &= \sum_{i=0}^{2n} W_i^{(c)} [Z_{i,k+1|k} - \bar{Z}_{k+1}][Z_{i,k+1|k} - \bar{Z}_{k+1}]^{\mathrm{T}} + R,\\
P_{x_k z_k} &= \sum_{i=0}^{2n} W_i^{(c)} [\boldsymbol{X}_{i,k+1|k} - \hat{\boldsymbol{X}}^*_{k+1}][Z_{i,k+1|k} - \bar{Z}_{k+1}]^{\mathrm{T}}.
\end{aligned}$$

(6) Calculate the Kalman gain matrix and update the state variables and covariance matrix.

$$\begin{aligned}
\mathcal{K}_{k+1} &= P_{x_k z_k} P^{-1}_{z_k z_k},\\
\hat{\boldsymbol{X}}_{k+1} &= \hat{\boldsymbol{X}}^*_{k+1} + \mathcal{K}_{k+1}[Z_{k+1} - \bar{Z}_{k+1}],\\
\boldsymbol{P}_{k+1} &= \boldsymbol{P}^*_{k+1} - \mathcal{K}_{k+1} P_{z_k z_k} \mathcal{K}^{\mathrm{T}}_{k+1}.
\end{aligned}$$

Note that the UKF method approximates the probability density distribution of the nonlinear function, approximates the sample states using a series of posterior probability densities, and preserves the high-order terms of the system. This method guarantees high precision and strong stability.

5 Simulation

This section analyzes the performance of the designed controller and observer in a simulation study. The gliding motion of the UGSR was simulated in MATLAB Simulink. The basic parameters of the system are given in Table 2.

The initial states of the system were set to $V = 0.1$ m/s, $\gamma = 0$, $\alpha = 0$, and $\omega_2 = 0$. The desired gliding path was described by $V_d = 0.3$ m/s and $\gamma_d = -25°$. To fix the mechanism limitation of the robot, the lower and upper bounds of the system input were set to -0.05 and 0.05 m, respectively. First, the LQR and SMC methods were compared to verify the closed-loop performance of the designed controller. The SMC control parameters were defined as $c_1 = 0.5$, $c_2 = 0.3$, $\epsilon_1 = 0.01$, $b_1 = 0.5$, $p_1 = 0.01$, $k_1 = 1$, $\epsilon_2 = 0.01$, $b_2 = 0.5$, $p_2 = 0.01$, and $k_2 = 1$. Figure 5 shows the system inputs, the gliding speed V, and the gliding path angle γ. The SMC reached steady state earlier than the LQR method, and achieved a smoother transition process.

Real fluids are affected by various disturbances that change their hydrodynamic coefficients. After 20 s of simulation and taking the disturbances from Yang et al. [29], the initial drag coefficient C_D was increased by 25%, and the initial lift coefficient C_L and torque coefficient C_M were reduced by 25%. The

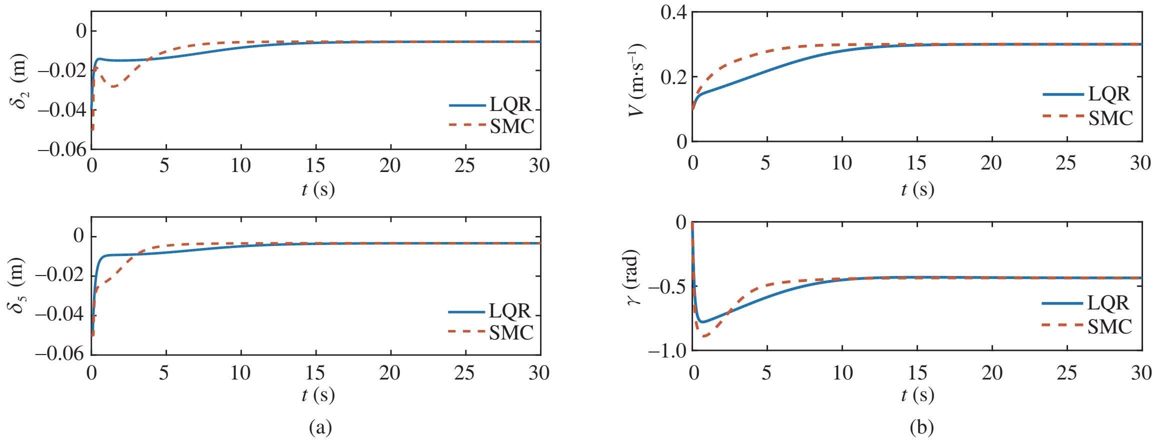

Figure 5 (Color online) Simulation of the SMC system. (a) System inputs δ_2 (top) and δ_5 (bottom); (b) gliding speed V (top) and gliding path angle γ (bottom).

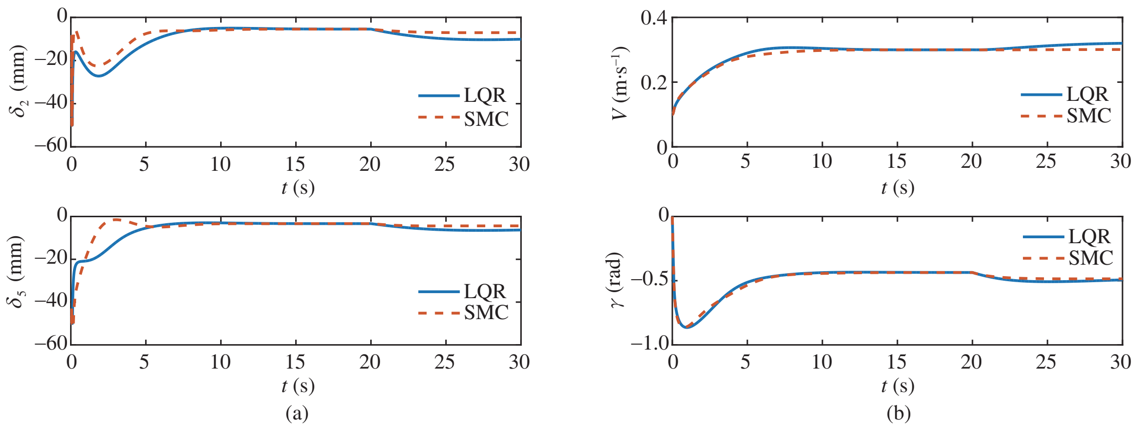

Figure 6 (Color online) Simulation of the SMC system under hydrodynamic coefficient disturbances. (a) System inputs δ_2 (top) and δ_5 (bottom); (b) gliding speed V (top) and gliding path angle γ (bottom).

simulation results of the closed-loop system with parameter disturbances are shown in Figure 6. Under the parameter perturbation, the state of the LQR system was significantly altered, whereas that of the SMC system was almost unchanged. This result confirms the robustness of the SMC controller against parameter uncertainty.

Next, the effect of input disturbance on the system was analyzed. The input noise was a random signal with a mean of zero and a variance of 0.001. Figure 7 shows the simulated system inputs and gliding states under the input disturbance. The SMC better reduced the influence of input noise on the system than the LQR method, and ensured stability of the system state within a smaller range, thus demonstrating the robustness of the controller against input noise.

To verify the state estimation capability of the UKF, the simulation results of the SMC system were compared with the UKF estimates. The original continuous nonlinear system was discretized by the Euler method with a sampling time of 0.005 s. The initial state of the UKF was defined as $\boldsymbol{X}_0 = [0.2, 0.1, 0.1, 0.1]^{\mathrm{T}}$, and the corresponding covariance was selected as $\boldsymbol{P}_0 = \mathrm{diag}\{0.05, 0.1, 0.1, 0.01\}$. The covariance of the measurement noise was $R = 0.01$ and the process noise was ignored. The parameters of the UKF algorithm were $a = 0.01$, $\kappa = 0$, and $\beta = 2$. Parameter uncertainties and input disturbances in the system were not considered. Figure 8 displays the simulated pitch angle θ and its estimation error, the gliding speed V, and the gliding path angle γ. The values can be measured by the attitude sensor, which integrates a gesture solver and obtains the pitch angle with measurement noise. The UKF accurately computed the pitch angle and achieved the state estimation based on the noisy measured data. The error between the estimation and simulation was within the allowable range, thereby validating the observer.

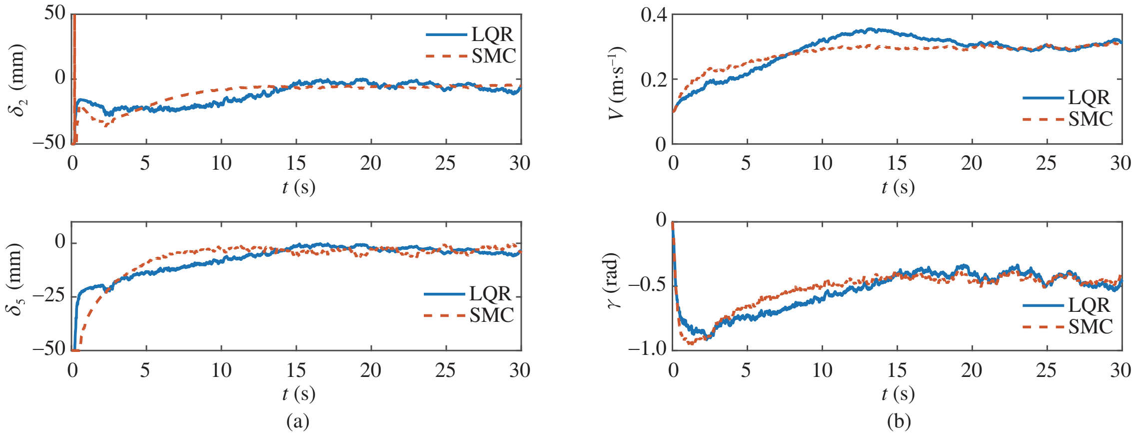

Figure 7 (Color online) Simulation of the SMC system under input disturbances. (a) System inputs δ_2 (top) and δ_5 (bottom); (b) gliding speed V (top) and gliding path angle γ (bottom).

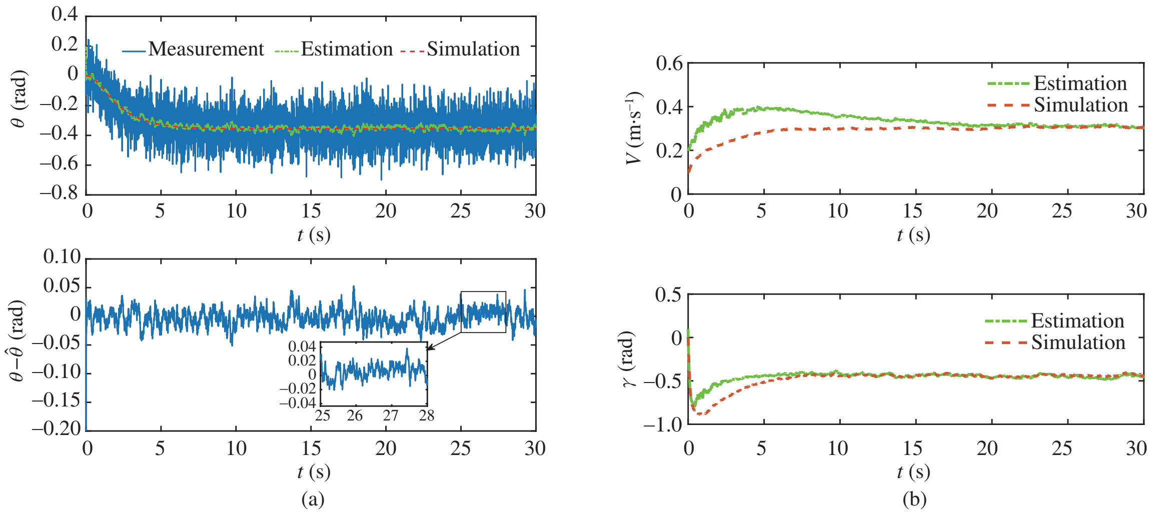

Figure 8 (Color online) UKF estimation of the SMC system with measurement noise. (a) Filtering result of pitch angle θ; (b) gliding speed V (top) and gliding path angle γ (bottom).

After verifying the proposed controller and observer, the UKF and SMC were combined into the overall system. The SMC parameters were chosen as $c_1 = 0.5$, $c_2 = 0.3$, $\epsilon_1 = 0.001$, $b_1 = 0.5$, $p_1 = 0.01$, $k_1 = 0.5$, $\epsilon_2 = 0.02$, $b_2 = 0.5$, $p_2 = 0.01$, and $k_2 = 1$. The covariance $\boldsymbol{P}_0$ was set to $\mathrm{diag}\{0.2, 0.1, 0.1, 0.01\}$. The remaining parameters of the system and UKF were those used in the previous simulation. Figure 9 presents the simulation results of the control law $\boldsymbol{u}$, the system inputs δ_2 and δ_5, the sliding surfaces, and gliding states. The results prove the effectiveness of the UKF-based SMC system.

6 Conclusion

This paper introduced the UGSR, which is based on underwater snake-like robots, but achieves gliding motion using telescopic modules. As gliding is an energy-efficient and long-duration motion mode driven by net buoyancy, the UGSR preserves the high mobility of the snake-like robot but demonstrates superior endurance ability. Considering the principles and characteristics of gliding motion, a dynamic model of the UGSR was established. The difficulty of tracking control was alleviated by an input-output linearization. Closed-loop stability of the nonlinear system was then achieved by an SMC design. This method effectively handled the influence of parameter uncertainty and disturbance on the system stability. As the control law is an expression of the module elongations, the actual system inputs were obtained by a

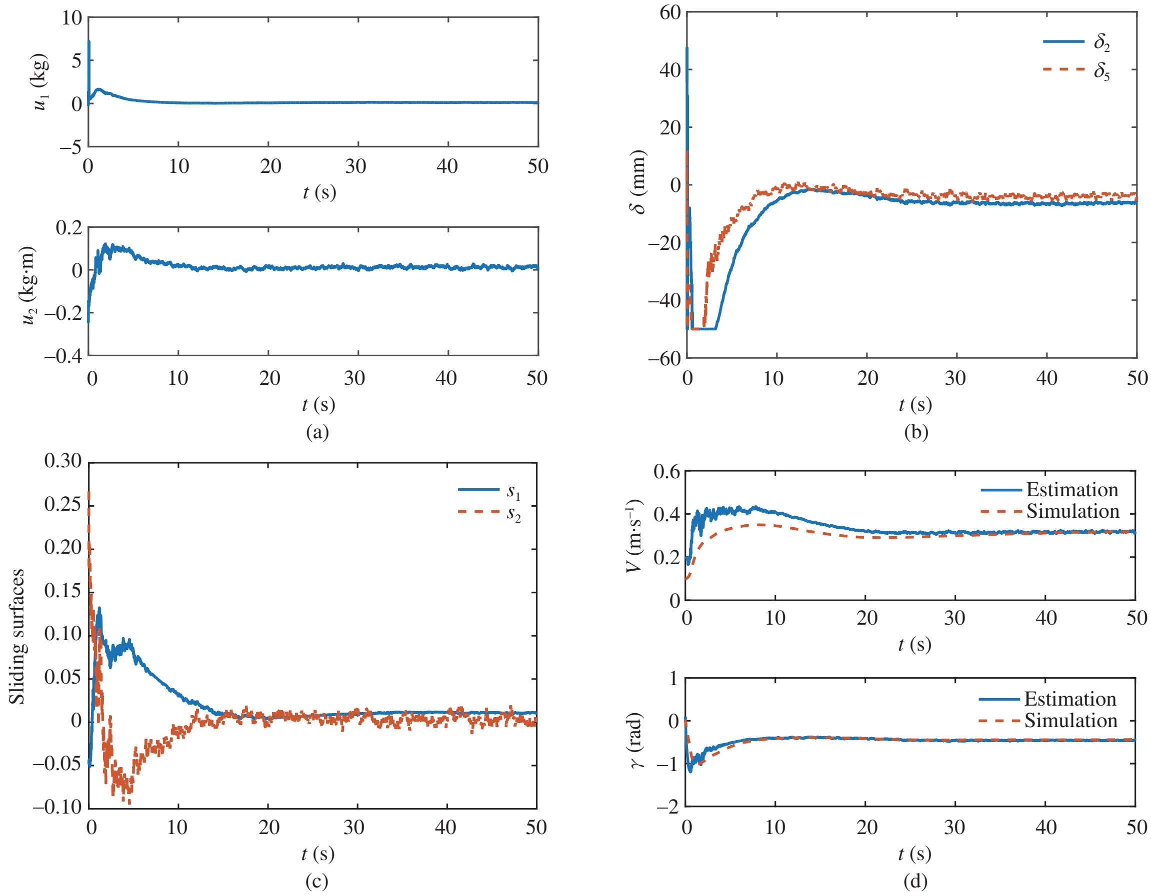

Figure 9 (Color online) Simulation of the UKF-based SMC closed-loop system. (a) Control law $\boldsymbol{u}$; (b) system inputs δ_2 and δ_5; (c) sliding surfaces s_1 and s_2; (d) gliding speed V (top) and gliding path angle γ (bottom).

decoupling solver. To implement the feedback control method, all states of the system must be input to the controller. Thus, a UKF based nonlinear observer was constructed to extract the noisy measurement signals and to estimate the state variables. Simulations verified the robustness of the proposed controller under hydrodynamic parameter disturbances and input disturbances, and demonstrated the state estimation accuracy and stability of the observer. Finally, the effectiveness of the UKF-based SMC system was confirmed.

In future work, the control method will be applied to a prototype, and the stability and state tracking of the gliding motion will be evaluated in a pool and lake test. Moreover, the hybrid dynamics of the UGSR will be studied to achieve yaw control of the gliding motion through the rotate modules.

Acknowledgements This work was supported by National Key Research and Development Project of China (Grant No. 2017YFB1300101).

References

1 Gomáriz S, Masmitjá I, González J, et al. GUANAY-II: an autonomous underwater vehicle for vertical/horizontal sampling. J Mar Sci Technol, 2015, 20: 81–93
2 Chen C W, Jiang Y, Huang H C, et al. Computational fluid dynamics study of the motion stability of an autonomous underwater helicopter. Ocean Eng, 2017, 143: 227–239
3 Webb D C, Simonetti P J, Jones C P. SLOCUM: an underwater glider propelled by environmental energy. IEEE J Ocean Eng, 2001, 26: 447–452
4 Sherman J, Davis R E, Owens W B, et al. The autonomous underwater glider "Spray". IEEE J Ocean Eng, 2001, 26: 437–446
5 Eriksen C C, Osse T J, Light R D, et al. Seaglider: a long-range autonomous underwater vehicle for oceanographic research. IEEE J Ocean Eng, 2001, 26: 424–436
6 Yu J C, Zhang A Q, Jin W M, et al. Development and experiments of the Sea-Wing underwater glider. China Ocean

Eng, 2011, 25: 721–736
7 Katzschmann R K, Marchese A D, Rus D. Hydraulic autonomous soft robotic fish for 3D swimming. In: Experimental Robotics. Berlin: Springer, 2016. 405–420
8 Park S J, Gazzola M, Park K S, et al. Phototactic guidance of a tissue-engineered soft-robotic ray. Science, 2016, 353: 158–162
9 Kelasidi E, Liljeback P, Pettersen K Y, et al. Innovation in underwater robots: biologically inspired swimming snake robots. IEEE Robot Autom Mag, 2016, 23: 44–62
10 Zhang A F, Ma S G, Li B, et al. Tracking control of tangential velocity of eel robot based on iterative learning control. Robot, 2018, 40: 769–778
11 Wu Z X, Yu J Z, Yuan J, et al. Towards a gliding robotic dolphin: design, modeling, and experiments. IEEE/ASME Trans Mech, 2019, 24: 260–270
12 Sverdrup-Thygeson J, Kelasidi E, Pettersen K Y, et al. The underwater swimming manipulator-a bio-inspired AUV. In: Proceedings of IEEE/OES Autonomous Underwater Vehicles (AUV), Tokyo, 2016. 387–395
13 Kelasidi E, Pettersen K Y, Liljebäck P, et al. Locomotion efficiency of underwater snake robots with thrusters. In: Proceedings of IEEE International Symposium on Safety, Security, and Rescue Robotics (SSRR), Lausanne, 2016. 174–181
14 Zhang F, En-Nasr O, Litchman E, et al. Autonomous sampling of water columns using gliding robotic fish: control algorithms and field experiments. In: Proceedings of IEEE International Conference on Robotics and Automation (ICRA), Washington, 2015. 517–522
15 Wu Z X, Yu J Z, Yuan J, et al. Mechatronic design and implementation of a novel gliding robotic dolphin. In: Proceedings of IEEE International Conference on Robotics and Biomimetics (ROBIO), Zhuhai, 2015. 267–272
16 Noh M M, Arshad M R, Mokhtar R M. Depth and pitch control of USM underwater glider: performance comparison PID vs. LQR. Indian J Geo-Mar Sci, 2011, 40: 200–206
17 Tchilian R S, Rafikova E, Gafurov S A, et al. Optimal control of an underwater glider vehicle. Procedia Eng, 2017, 176: 732–740
18 Moon J H, Jee S C, Lee H J. Output-feedback control of underwater gliders by buoyancy and pitching moment control: feedback linearization approach. Int J Control Autom Syst, 2016, 14: 255–262
19 Sang H Q, Zhou Y, Sun X J, et al. Heading tracking control with an adaptive hybrid control for under actuated underwater glider. ISA Trans, 2018, 80: 554–563
20 Liu J C, Wu Z X, Yu J Z, et al. Sliding mode fuzzy control-based path-following control for a dolphin robot. Sci China Inf Sci, 2018, 61: 024201
21 Zhang Z, Wang F, Guo Y, et al. Multivariable sliding mode backstepping controller design for quadrotor UAV based on disturbance observer. Sci China Inf Sci, 2018, 61: 112207
22 Pukdeboon C. Extended state observer-based third-order sliding mode finite-time attitude tracking controller for rigid spacecraft. Sci China Inf Sci, 2019, 62: 012206
23 Gao W B, Hung J C. Variable structure control of nonlinear systems: a new approach. IEEE Trans Ind Electron, 1993, 40: 45–55
24 Zhang F T, Tan X B. Nonlinear observer design for stabilization of gliding robotic fish. In: Proceedings of American Control Conference, Portland, 2014. 4715–4720
25 Yuan J, Wu Z X, Yu J Z, et al. Sliding mode observer-based heading control for a gliding robotic dolphin. IEEE Trans Ind Electron, 2017, 64: 6815–6824
26 Julier S J, Uhlmann J K. Unscented filtering and nonlinear estimation. Proc IEEE, 2004, 92: 401–422
27 Aghababa M P, Akbari M E. A chattering-free robust adaptive sliding mode controller for synchronization of two different chaotic systems with unknown uncertainties and external disturbances. Appl Math Comput, 2012, 218: 5757–5768
28 Ioannou P A, Sun J. Robust Adaptive Control. Upper Saddle River: Prentice-Hall, 1996
29 Yang H, Ma J. Sliding mode tracking control of an autonomous underwater glider. In: Proceedings of International Conference on Computer Application and System Modeling (ICCASM), Taiyuan, 2010. 555–558